



HAL
open science

Physical Limits to Human Brain B0 Shimming, and Engineering Implications

Bruno Pinho Meneses, Alexis Amadon

► **To cite this version:**

Bruno Pinho Meneses, Alexis Amadon. Physical Limits to Human Brain B0 Shimming, and Engineering Implications. 2021. hal-03210241v1

HAL Id: hal-03210241

<https://hal.science/hal-03210241v1>

Preprint submitted on 27 Apr 2021 (v1), last revised 6 Dec 2021 (v2)

HAL is a multi-disciplinary open access archive for the deposit and dissemination of scientific research documents, whether they are published or not. The documents may come from teaching and research institutions in France or abroad, or from public or private research centers.

L'archive ouverte pluridisciplinaire **HAL**, est destinée au dépôt et à la diffusion de documents scientifiques de niveau recherche, publiés ou non, émanant des établissements d'enseignement et de recherche français ou étrangers, des laboratoires publics ou privés.

Physical Limits to Human Brain B₀ Shimming, and Engineering Implications

Bruno Pinho Meneses¹ | Alexis Amadon, PhD¹

¹Universite Paris-Saclay, CEA, CNRS, BAOBAB, NeuroSpin, 91191 Gif-sur-Yvette, France

Correspondence

Alexis Amadon PhD, Universite Paris-Saclay, CEA, CNRS, BAOBAB, NeuroSpin, 91191 Gif-sur-Yvette, France
Email: alexis.amadon@cea.fr

Funding information

CFR Grant from the Commissariat a l'Energie Atomique et aux Energies Alternatives (CEA)

As the main magnetic field in MRI scanners increases to provide improved intrinsic SNR, susceptibility-induced B₀-inhomogeneity increases proportionally, aggravating related artifacts. Although optimized shimming equipment can mitigate them, we demonstrate in this work that depending on the field source distribution around a region of interest, no shimming hardware external to such a zone can fully mitigate the inhomogeneous field, which is shown to be the case for the human brain. Thus, solid (spherical) harmonic shimming simulations of very high degree are performed on a large 100-subject database of B₀-fieldmaps, establishing a 12.3 Hz inhomogeneity hard shim limit at 7 T for whole brain shimming, which can only be attained at shimming degree higher than 90. On the other hand, under limited resources (i.e., max power dissipation, shimming degree), 3D region-specific shimming is shown to be a very effective way to improve homogeneity in critical zones such as the pre-frontal cortex and around ear canals. Finally, perfect shimming of a ROI is shown to be possible as long as the ROI can be contained within a sphere that does not enclose sources of magnetic field inhomogeneity.

Abbreviations: CNR, Contrast-to-Noise Ratio; DBM, Dipole Boundary Method; EPI, Echo-Planar Imaging; fMRI, functional MRI; FOV, Field of View; FSE, Fast Spin Echo; GRE, Gradient Recalled Echo; ISH, Irregular Solid Harmonics; MCA, Multi-Coil Array; MP-RAGE, Magnetization-Prepared Rapid Acquisition with Gradient Echo; PFC, Prefrontal Cortex; ROI, Region of Interest; RSH, Regular Solid Harmonics; SF, Stream Function; SH, Spherical Harmonics; SNR, Signal-to-Noise Ratio; SO-SF, Subject-Optimal Stream Function; SSFP, Steady-State Free Precession; TL, Temporal Lobe; UHF, Ultra-High Field.

KEYWORDS

B0 Shimming, Human Brain Shimming, Solid Harmonics, Spherical Harmonics, Ultra High Field, Shim Coil Design, Susceptibility-Induced Inhomogeneity, Magnetic Resonance Imaging.

1 | INTRODUCTION

When immersed in the uniform magnetic field B_0 of the MRI scanner, the media composing the human head (biological tissue, air) become magnetized, in turn generating a non-uniform magnetic field distribution $\delta B_0(x)$ obeying

$$\nabla^2 \delta B_0 = \left(\nabla^2 \chi - 3 \frac{\partial^2 \chi}{\partial z^2} \right) \frac{B_0}{3}, \quad (1)$$

(adapted from Salomir *et al.* 2003¹) where $\chi(x)$ is the media's magnetic susceptibility.

Such inhomogeneous magnetic field distribution is at the origin of several kinds of image artifacts in human brain imaging, with geometric distortion in Echo Planar acquisitions being a notorious example²⁻⁷.

As an example, in non-accelerated EPI single-shot acquisitions, under 0.5 ms inter-echo spacing and 200 mm Field-of-View (FOV) in the phase encoding direction, a 100 Hz excursion in the magnetic field leads to 10 mm geometric distortion in the reconstructed image³⁻⁵. It is therefore not surprising that appreciable effort has been directed to the design of shimming systems for the human brain⁸⁻¹³, but as we will see, they are still far from achieving the minimal inhomogeneity.

Other B_0 related complications are signal loss in T_2^* -weighted imaging⁵, banding artefacts in Steady-State Free Precession (SSFP) sequences¹¹, failed inversion-recovery pulse, inhomogeneous flip angle distribution¹⁴, and line broadening in spectroscopy¹⁵.

With the current trend of increasing magnetic field intensity of clinical and research MRI scanners (7 T Siemens Terra, 10.5 T at the Center for Magnetic Resonance Research (CMRR)¹⁶, 11.7 T Iseult project¹⁷) to achieve higher Signal-to-Noise Ratio (SNR) and Contrast-to-Noise Ratio (CNR), susceptibility-induced inhomogeneity rises proportionally to the main field. High performance static field shimming becomes crucial for these scanners to deliver their full potential in applications such as functional MRI (fMRI)¹⁸.

Correction of inhomogeneous fields is either active, generated by electric current flow in conductors located around the patient, or passive, by the placement of ferromagnetic pieces in optimal positions¹⁹⁻²¹. This subject specific shimming is performed in clinical routine by Spherical Harmonics (SH) based systems integrated to the MRI scanner, commonly of 2nd degree and eventually up to 3rd degree. To improve shimming performances, higher-degree SH-based systems have also been employed²², containing up to partial 5th degree. Moreover, non-SH-based Multi-Coil Array (MCA) systems^{8;9;23;24} have gained traction in the last years. These have been shown to provide adequate homogeneity for numerous applications at Ultra High Field (UHF), particularly in dynamic shimming mode^{8;10}, but strong field excursions persist around the ear canals and in the pre-frontal cortex despite shimming, even when employing brain-optimized MCAs^{11-13;25-27}.

Aware of these unmet needs, we first analyze and demonstrate why perfect shimming of an entire human brain is impossible, based on theory and topological considerations. Then we explore the limits of B_0 shimming through unconstrained SH shimming simulations on a large database of brain 3D fieldmaps. Furthermore, assessment of realistic

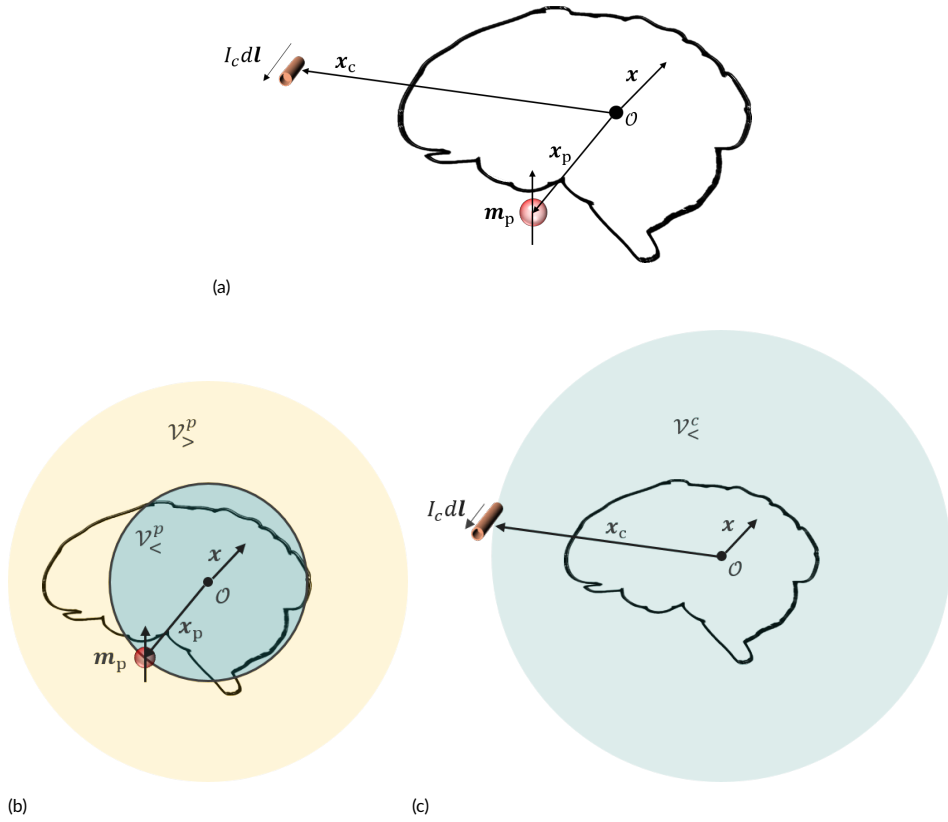


FIGURE 1 (a) Disposition of fundamental building blocks for sample-induced magnetic field perturbation (m_p) and field correction ($I_c dl$) around the brain. The MR magnet isocenter at O corresponds to the origin of the B_0 SH-decomposition. Vector $x \in \mathbb{R}^3$ points to an arbitrary brain voxel to be shimmed. (b) A representation of the regions where the magnetic field generated by a punctual sample-induced perturbation is described by RSH ($V_{<}^p$) and ISH ($V_{>}^p$). (c) The region $V_{<}^c$ where the correction magnetic field is decomposed into RSH.

shim systems is performed through power constrained coil design, where homogeneity levels attained by such systems will be compared to the lowest achievable homogeneity. Knowledge of the attainable levels of homogeneity for diverse shimming strategies (whole-brain, region-specific, slice-wise) can provide meaningful insight for future shim system design, since for limited resources (channel count, maximum current and power), a region-specific shimming strategy could provide homogeneity levels unattainable when applying global (whole-brain) shimming.

2 | THEORY: PHYSICAL LIMITS TO B0 SHIMMING

B_0 homogeneity in the human brain is mainly disturbed by the presence of susceptibility gradients between paramagnetic air cavities and diamagnetic tissues, as described in equation 1. This perturbation can be seen as caused by a distribution of magnetic dipoles oriented in the B_0 field direction and located on air-tissue interfaces. For the human head, a distribution of dipole moments disturbing the once uniform magnetic field appears, located around the ear

canals, sinus, mouth and any other interface with non-negligible susceptibility difference. Susceptibility differences also exist between white matter, gray matter and cerebrospinal fluid, but are less significant in comparison to that between air and tissues, and are considered negligible in this work.

Although there are mentions in the literature to the impossibility of perfectly shimming the magnetic field inside the brain²⁸, no detailed account on the reason for such limitation has been provided.

In the subsequent analysis, the reference coordinate frame is defined such that axes x , y and z are oriented in the subject's PA, RL and FH directions, respectively, assuming the patient lies on his back. The main B_0 field is oriented in the positive z direction.

2.1 | Laplace's Equation and Solid Harmonics

Any magnetic field in a source-free region obeys Laplace's equation. In the z direction one obtains:

$$\nabla^2 B_z(r, \theta, \varphi) = 0. \quad (2)$$

This equation has general solution given by

$$B_z(r, \theta, \varphi) = \sum_{n=0}^{+\infty} \sum_{m=-n}^n A_n^m \mathcal{R}_n^m(r, \theta, \varphi) + B_n^m \mathcal{I}_n^m(r, \theta, \varphi) \quad (3)$$

with

$$\mathcal{R}_n^m(r, \theta, \varphi) = r^n Y_n^m(\theta, \varphi), \quad (4)$$

$$\mathcal{I}_n^m(r, \theta, \varphi) = \frac{1}{r^{n+1}} Y_n^m(\theta, \varphi) \quad (5)$$

and

$$Y_n^m(\theta, \varphi) = \begin{cases} P_n^m(\cos \theta) \cos m\varphi & m \geq 0 \\ P_n^{|m|}(\cos \theta) \sin |m|\varphi & m < 0 \end{cases}, \quad (6)$$

where \mathcal{R}_n^m , \mathcal{I}_n^m and Y_n^m are denominated Regular Solid Harmonic (RSH), Irregular Solid Harmonic (ISH) and Spherical (or Surface) Harmonic (SH), respectively, of degree n and order m ; and functions $P_n^m : [-1, 1] \rightarrow \mathbb{R}$ are Associated Legendre Polynomials given by

$$P_n^m(x) = \frac{(1-x^2)^{\frac{m}{2}}}{2^n n!} \frac{d^{n+m}}{dx^{n+m}} (x^2-1)^n. \quad (7)$$

Using the above definitions for RSH and ISH, the particular Green function for the Laplacian, $1/|\mathbf{x} - \mathbf{x}'|$, present in the formulas of scalar and vector magnetic potentials in magneto-statics, can be expanded into (adapted from Jackson, 2007²⁹):

$$\frac{1}{|\mathbf{x} - \mathbf{x}'|} = \sum_{n=0}^{+\infty} \sum_{m=0}^n (2 - \delta_{m0}) \frac{(n-m)!}{(n+m)!} \frac{r_{<}^n}{r_{>}^{n+1}} P_n^m(\cos \theta) P_n^m(\cos \theta') \cos m(\varphi - \varphi') \quad (8)$$

with $r_{>}$ ($r_{<}$) the larger (smaller) between $|\mathbf{x}|$ and $|\mathbf{x}'|$; and δ_{m0} the Kronecker delta.

2.2 | Mathematical Analysis of Magnetic Field Sources Around the Brain

From equation 1, the inhomogeneous magnetic field appearing once the patient is immersed in the main B_0 field is caused by a distribution of magnetic dipoles located on air-tissue interfaces. As such, an infinitesimal magnetic dipole can be considered as a fundamental building-block to analyze the sample-induced B_0 inhomogeneity, defined as the B_0 standard deviation to mean ratio across the Region-Of-Interest (ROI).

To counteract the inhomogeneous magnetic field, active shimming systems are commonly employed, and an infinitesimal current filament can be used as another fundamental building block to describe the magnetic field of such systems.

Both fundamental pieces are depicted in Fig. 1. The perturbation is produced by a magnetic dipole of moment $\mathbf{m}_p = m_p \hat{z}$, located at some arbitrary location \mathbf{x}_p with spherical coordinates $(r_p, \theta_p, \varphi_p)$; and the correction field is produced by a wire filament carrying current I_c , with length dL , located at \mathbf{x}_c with spherical coordinates $(r_c, \theta_c, \varphi_c)$ relative to SH isocenter O .

2.2.1 | Solid Harmonic Expansion of Sample Induced Perturbation

To analyze the magnetic field generated by \mathbf{m}_p inside the brain, it is convenient to employ the magnetic scalar potential, given by:

$$\Phi_p(\mathbf{x}) = -\frac{\mathbf{m}_p}{4\pi} \cdot \nabla \frac{1}{|\mathbf{x} - \mathbf{x}_p|}. \quad (9)$$

From $\mathbf{B} = -\mu_0 \nabla \Phi$, the magnetic field in the z direction is

$$B_z^p(\mathbf{x}) = \frac{\mu_0 m_p}{4\pi} \frac{\partial^2}{\partial z^2} \frac{1}{|\mathbf{x} - \mathbf{x}_p|}. \quad (10)$$

Substituting 8 into 10, according to the position of the point of interest \mathbf{x} relatively to \mathbf{x}_p , one obtains two possible expressions for the magnetic field. Those are:

$$B_z^p(\mathbf{x}) = \frac{\mu_0 m_p}{4\pi r_p^3} \sum_{n=0}^{+\infty} \sum_{m=0}^n (2 - \delta_{m0}) \frac{(n-m+2)!}{(n+m)!} \frac{P_{n+2}^m(\cos \theta_p)}{r_p^n} r^n P_n^m(\cos \theta) \cos m(\varphi - \varphi_p), \quad (11)$$

in $\mathcal{V}_{<}^p = \{\mathbf{x} \in \mathbb{R}^3 : |\mathbf{x}| < r_p\}$, and

$$B_z^p(\mathbf{x}) = \frac{\mu_0 m_p}{4\pi} \sum_{n=2}^{+\infty} \sum_{m=0}^{n-2} \frac{(2 - \delta_{m0})(n-m)!}{(n+m-2)!} P_{n-2}^m(\cos \theta_p) \frac{r_p^{n-2}}{r^{n+1}} P_n^m(\cos \theta) \cos m(\varphi - \varphi_p) \quad (12)$$

in $\mathcal{V}_>^p = \{\mathbf{x} \in \mathbb{R}^3 : |\mathbf{x}| > r_p\}$. Equation 11 was adapted from Romeo & Hoult, 1984¹⁹, and equation 12 can be derived in a similar fashion.

We notice, therefore, that in $\mathcal{V}_<^p$ the magnetic field is composed exclusively of RSH, while ISH describe the magnetic field in $\mathcal{V}_>^p$. Moreover, let \mathcal{V}_b be the brain region, the sample induced perturbations can produce both RSH and ISH fields in its interior as long as the intersection of \mathcal{V}_b with sets $\mathcal{V}_<^p$ and $\mathcal{V}_>^p$ is non-null.

2.2.2 | Solid Harmonic Expansion of Correction Fields

With the inhomogeneous field described, we move our attention to the correction fields. The filament chosen as building-block for correction devices has magnetic vector potential given by

$$d\mathbf{A}_c(\mathbf{x}) = \frac{\mu_0 I_c d\mathbf{l}}{4\pi} \frac{1}{|\mathbf{x} - \mathbf{x}_c|} \quad (13)$$

producing

$$dB_z^c(\mathbf{x}) = \hat{\mathbf{z}} \cdot (\nabla \times d\mathbf{A}_c(\mathbf{x})) \quad (14)$$

as magnetic field in the z direction.

Substitution of 8 into 13 and subsequent calculation of 14 leads to (adapted from Romeo & Hoult, 1984¹⁹)

$$dB_z^c(r, \theta, \phi) = \frac{\mu_0 I_c \sin \theta_c d\varphi}{4\pi} \sum_{n=0}^{+\infty} \sum_{m=0}^{n+1} \left[\frac{(n-m)!}{(n+m)!} \frac{P_{n+1}^{m+1}(\cos \theta_c)}{r_c^{n+1}} - \frac{(n-m+2)!}{(n+m)!} \frac{P_{n+1}^{m-1}(\cos \theta_c)}{r_c^{n+1}} \right] \times r^n P_n^m(\cos \theta) \cos m(\varphi - \varphi_c). \quad (15)$$

in $\mathcal{V}_<^c = \{\mathbf{x} \in \mathbb{R}^3 : |\mathbf{x}| < r_c\}$.

As the shimming system is positioned around the patient's body or head, we have $\mathcal{V}_b \subset \mathcal{V}_<^c$; therefore, equation 15 is sufficient for describing the magnetic field in the subject's brain generated by shimming structures, and it is observed that this magnetic field only generates RSH.

2.2.3 | Condition for Perfect B0 Shimming

RSH and ISH functions are linearly independent. Therefore, any shimming apparatus placed around the head can only zero-out the sample-induced inhomogeneity in the brain if $\mathcal{V}_>^p \cap \mathcal{V}_b = \emptyset$, i.e. there is no ISH term describing the magnetic field inside the brain. Or, stated in a simpler and generalized form, a region within an anatomy can only be shimmed to a perfectly homogeneous magnetic field by an external shimming apparatus if, and only if, the smallest sphere enclosing said region does not contain any source of magnetic field.

3 | METHODS

We start by showing that the human brain does not satisfy the condition for perfect B₀ homogenization. Then, by performing RSH shimming in a large database of δB_0 fieldmaps, the minimal inhomogeneity theoretically achievable σ_{\min} is estimated. In addition, we discuss how state-of-the-art shimming systems compare to the best achievable

inhomogeneity. Different regions of interest are explored in this phase to compare global, slice-by-slice and slab-specific shimming.

Finally, the estimated ultimate inhomogeneity is compared to what could be achieved by optimal shim coils under power constraints.

3.1 | Source Localization in a 3D Head Model

Using a 3D model of the human head³⁰, with magnetic susceptibilities of air and tissues set to $\chi_a = 0.36 \times 10^{-6}$ and $\chi_t = -9.03 \times 10^{-6}$, respectively, the magnetic field source distribution around it is computed from the right side of equation 1:

$$\rho_m(\mathbf{x}) = \left(\nabla^2 \chi - 3 \frac{\partial^2 \chi}{\partial z^2} \right) \frac{B_0}{3}. \quad (16)$$

Once ρ_m is known, the set $\mathcal{X} = \{|\mathbf{x}| : \rho_m(\mathbf{x}) \neq 0\}$ can be defined. Let $\mathcal{B}(\text{inf } \mathcal{X}, O)$ be a ball¹ of radius $\text{inf } \mathcal{X}$, centered at O , according to our proposition, if $\mathcal{B} \cap \mathcal{V}_b \neq \mathcal{V}_b$, the brain cannot be perfectly shimmed by RSH. Nevertheless, $\mathcal{B}(\text{inf } \mathcal{X}, O)$ or any other ball inside the brain (not necessarily centered at O), not enclosing magnetic field sources, could still be perfectly shimmed.

3.2 | Ultra-High-Degree Simulation of RSH Shimming

To determine the best achievable homogeneity under the theoretical limits, unconstrained RSH shimming simulations with increasing degree were performed on a 100-subject database of three dimensional δB_0 maps in the brain.

The database was built from fieldmaps acquired on a MAGNETOM Prisma 3 T imager (Siemens Healthcare GmbH, Erlangen, Germany) with 1.7 mm isotropic resolution, after 2nd degree shimming. FSL's brain extraction tool³¹ was used for masking and restrict our analysis to the human brain. Fieldmap acquisitions were performed with two 3D gradient echo sequences, one with 2 distant echoes $TE_1 = 1.88$ ms and $TE_3 = 4.9$ ms, and one with a single echo at $TE_2 = TE_1 + 0.7$ ms. TE_1 and TE_2 are supposed to be close enough in time so that no phase excursion occurs in the brain beyond $\pm\pi$ during that 0.7 ms interval (assumption: δB_0 does not exceed ± 714 Hz in the brain at 3T). Then a double-point linear fit of the phase evolution between TE_1 and TE_2 is initially performed for phase unwrapping of the last echo; then a triple-point linear fit of the phase evolution is performed for δB_0 estimation. The resulting δB_0 maps were cleaned with an outlier filter to avoid singularities, especially at the edge of the brain. It was then scaled up by 7/3 for investigation at 7T.

For the shimming simulations, given a target magnetic field $\mathbf{b} \in \mathbb{R}^K$ across K voxels, the vector $\mathbf{a} \in \mathbb{R}^{N^2+2N+1}$ of regular solid harmonic coefficients A_n^m for each degree $n = 1, \dots, N$, with N the RSH degree employed in the simulation, is computed such that

$$\mathbf{a} = \underset{\mathbf{a} \in \mathbb{R}^{N^2+2N+1}}{\text{argmin}} \quad \|\mathbf{b} - \mathbf{R}\mathbf{a}\|_2^2, \quad (17)$$

¹A ball $\mathcal{B}(R, \mathbf{c})$ of radius R centered at $\mathbf{c} \in \mathbb{R}^3$ is defined as the set of $\mathbf{x} \in \mathbb{R}^3$ such that $|\mathbf{x} - \mathbf{c}| < R$.

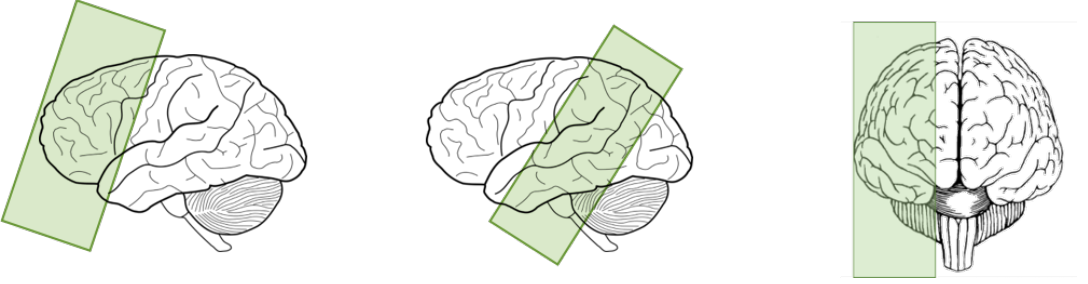


FIGURE 2 Slab positioning for localized shimming simulations with RSH and SO coil design. Targets from left to right: prefrontal cortex, temporal lobes (bilateral) and temporal lobe (unilateral).

with $\mathbf{R} \in \mathbb{R}^{K, N^2+2N+1}$ of the form

$$\mathbf{R} = \begin{bmatrix} \mathcal{R}_0^0(\mathbf{x}_1) & \mathcal{R}_1^{-1}(\mathbf{x}_1) & \mathcal{R}_1^0(\mathbf{x}_1) & \dots & \mathcal{R}_n^m(\mathbf{x}_1) & \dots & \mathcal{R}_N^N(\mathbf{x}_1) \\ \mathcal{R}_0^0(\mathbf{x}_2) & \mathcal{R}_1^{-1}(\mathbf{x}_2) & \mathcal{R}_1^0(\mathbf{x}_2) & \dots & \mathcal{R}_n^m(\mathbf{x}_2) & \dots & \mathcal{R}_N^N(\mathbf{x}_2) \\ \vdots & \vdots & \vdots & \ddots & \vdots & \ddots & \vdots \\ \mathcal{R}_0^0(\mathbf{x}_K) & \mathcal{R}_1^{-1}(\mathbf{x}_K) & \mathcal{R}_1^0(\mathbf{x}_K) & \dots & \mathcal{R}_n^m(\mathbf{x}_K) & \dots & \mathcal{R}_N^N(\mathbf{x}_K) \end{bmatrix}. \quad (18)$$

The inverse problem is solved using MATLAB's (The Mathworks, Natick, MA, USA) *lsqminnorm*.

For each subject, RSH shimming was performed targeting different types of brain regions: global, slice-by-slice and slab-specific. Slice-by-slice implies dynamic shimming of 1.7 mm transverse slices covering the whole-brain. Slab-specific shimming was performed considering three different slabs containing notoriously challenging regions to shim, namely the prefrontal cortex (PFC) and the temporal lobes (TLs). Temporal lobe shimming was further subdivided into two slab types: bilateral and unilateral. The choice of using slabs rather than employing precise segmentation of the regions of interest was made to account for common research and clinical practices. Slab masks were created manually for each subject with approximate thickness of 55 mm. Shimming is performed on the voxels in the intersection of the slab with the brain mask. The targeted slab characteristics are shown in Fig.2.

3.3 | Verification of the conditions for ultimate shimming

Considering a single, randomly selected subject from the database, validation of the condition for perfect shimming is performed by defining a spherical region enclosing critical inhomogeneity zones located in the ventral area of the prefrontal cortex, but not enclosing any obvious magnetic field sources (air cavities). RSH shimming of increasing degree is performed inside this ROI and it is compared to the achieved inhomogeneity for the same subject under global shimming. The spherical ROI is then shifted downward along the Head-Feet direction, and RSH shimming is applied on the voxels in the intersection of the brain mask with the ROI (\rightarrow truncated sphere). If the proposed condition for ultimate shimming is consistent, the sphere entirely located inside the brain should provide better homogeneity than the subsequent truncated spheres. The spherical ROI has 38 mm radius and is shown in Fig.9.

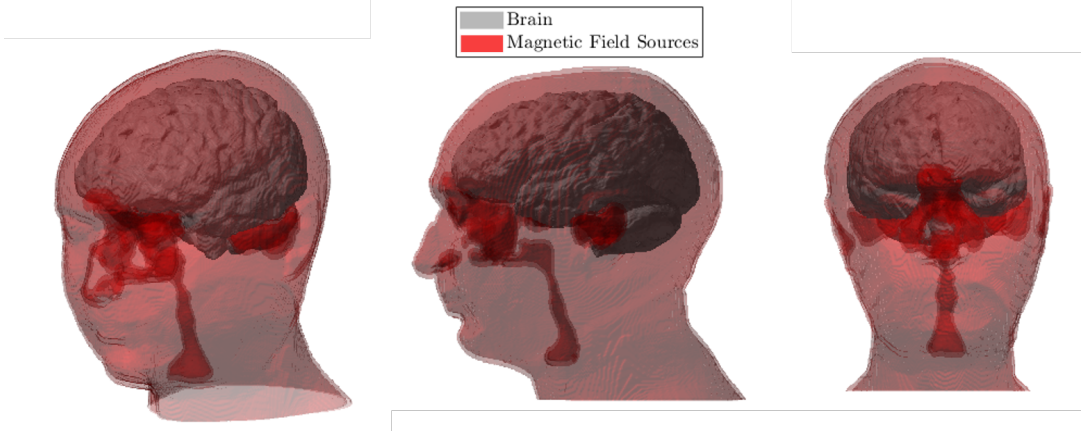


FIGURE 3 Magnetic field source disposition around the human brain as computed from equation 16.

3.4 | Comparison to optimal shim coil design

In order to explore practical aspects of coil design, and how realistic cylindrical systems could perform relatively to the best achievable inhomogeneity, the Dipole Boundary Method (DBM)¹³ is applied to compute subject-optimal stream-functions (SO-SFs) for each subject in the database under global and slab-specific shimming techniques.

SO-SFs are computed under different power dissipation targets to assess how performances relative to the best achievable homogeneity estimated from RSH shimming simulations are impacted by engineering limitations.

The SO-SFs are calculated over a cylindrical coil former of 140 mm radius, 300 mm length, with a 4 mm discretization step. Discretization into windings is performed with 2.4 mm minimum inter-wire spacing and copper wire of 1.54 mm² circular section. Power dissipation for each coil is then calculated for the obtained winding pattern. Target power for the designs are 3 W, 7 W, 15 W, 25 W, 50 W, 75 W and 100 W.

Inhomogeneity levels resulting from subject optimal designs are assessed and compared to very high-degree RSH shimming limits.

4 | RESULTS AND DISCUSSION

4.1 | Magnetic Field Perturbation Sources in the Human Head

The disposition of points \mathbf{x} satisfying $\rho_m(\mathbf{x}) \neq 0$ is shown in Fig. 3. A build-up of susceptibility-induced field sources is observed on the interface between the head and the surrounding air. Closer to the brain are the susceptibility-induced sources caused by susceptibility gradients between air cavities in the head (sinus and ear canals) and biological tissues. It is also apparent that, under the displayed configuration, the condition for perfect shimming cannot be fulfilled as the ball $\mathcal{B}(\inf X, O)$ will not enclose the brain. Or, alternatively, it is impossible to obtain any brain-enclosing sphere that does not enclose perturbation sources

The distribution of perturbation sources estimated from 16 is compatible with the strong inhomogeneous magnetic field commonly observed in the temporal lobes and frontal lobe. These inhomogeneity hotspots are discussed throughout a vast literature, from simulated^{28;32;33} to measured data^{34;35}. Due to the proximity of the sources to the brain, intense magnetic field values appear in the brain cortex, reaching values as high as 800 Hz at 7 T, as gathered

from the database.

4.2 | Whole-brain B0 Homogeneity Limits

The results for human brain shimming with very high RSH degree are shown in Fig. 4. Baseline inhomogeneity across the database is 65.7 Hz (SD: 11.4 Hz). As RSH degree increases, a steep inhomogeneity drop is observed up to 20th degree, with the rate of improvement of 1.5 Hz per degree when around 10th degree and a contrasting slower improvement afterwards, with only 0.07 Hz per degree around 70th degree. Due to limited computational resources and time, the maximum RSH degree was increased up to 90, presenting inhomogeneity of 15.9 Hz (SD: 3.4 Hz) in the brain, or an improvement of 75.8% relative to baseline.

Consistent with theoretical developments, an asymptotic behavior, tending to non-zero inhomogeneity, can be inferred from the inhomogeneity evolution. The minimum inhomogeneity achievable in the database could be extrapolated using MATLAB's *Curve Fitting Tool*, providing an average 12.3 Hz (95% Confidence Bounds: 10.9 Hz–13.7 Hz) for the database. This value represents an 81.3% improvement in homogeneity in the human brain. In theory, this result indicates that inhomogeneity at UHF of 7 T and 11.7 T could be reduced to the equivalent of 1.4 T and 2.4 T MRI systems, respectively, although the practical implementation of such a system is very unlikely.

Regarding the voxels presenting absolute field excursion superior to 100 Hz, which would account for stronger B_0 related artifacts, it follows a similar trend to that of the inhomogeneity, reaching a virtually artifact-free configuration, as an average of less than 0.5% of voxels over 100 Hz is achieved. This reduction is dramatic relatively to the initial proportion of 7.8%, which may cause information in a non-negligible portion of the brain to be lost in an EPI scan, for instance.

A more detailed visualization of how increasing RSH degrees act to reduce global inhomogeneity is provided in Fig. 5, where the evolution of the maximum $|\delta B_0|$ for the 80, 90, 95 and 98% voxels with lowest absolute excursion is shown. At relatively lower degrees, RSH functions act over all frequency ranges. As the correction degree increases, RSH action seems to be localized, as significant changes are mostly observed in the 95 and 98% ranges, thus on a smaller amount of voxels.

Fig. 6 shows that strong inhomogeneity regions still remain even after global shimming at very high degree. And although inhomogeneity values at very high degree present a significant drop from baseline inhomogeneity, most shim systems presented in the literature have shown performances at most equivalent to 6th degree RSH despite optimization of MCA loops placement and geometry in some studies^{11;27;36}.

In slice-by-slice shimming (cf Fig. 4b), inhomogeneity reduction as RSH degree increases is much greater. Inhomogeneity at 17th degree is 12.6 Hz (SD: 3.4 Hz), and already inferior to the inhomogeneity at 90th degree in global shimming. Voxels over 100 Hz are reduced to 0.2% (SD: 0.1%). The greater effectiveness of dynamic slice-by-slice shimming in mitigating B_0 inhomogeneity when compared to global shimming is known^{8;37}, and it is what makes it appealing for 2D acquisition schemes. From the results, we see that such a feature is linked to the lower RSH degree required, which indicates that less rapid spatial field variation is needed. From a shim system design perspective, given some surface upon which wire patterns will be placed, being able to generate rapidly spatially varying fields means putting as many loops as possible covering the whole surface. These RSH simulations indicate that the same spatial distribution of coils in a Multi-Coil Array will be able to perform better in slice-by-slice shimming compared to global shimming due to the need of lower degree RSH. While an efficient technique for reducing inhomogeneity, if isotropic submillimeter resolution is desired, 2D acquisition of very thin slices might not provide sufficient SNR. Three-dimensional acquisitions become necessary, and global shimming could be required.

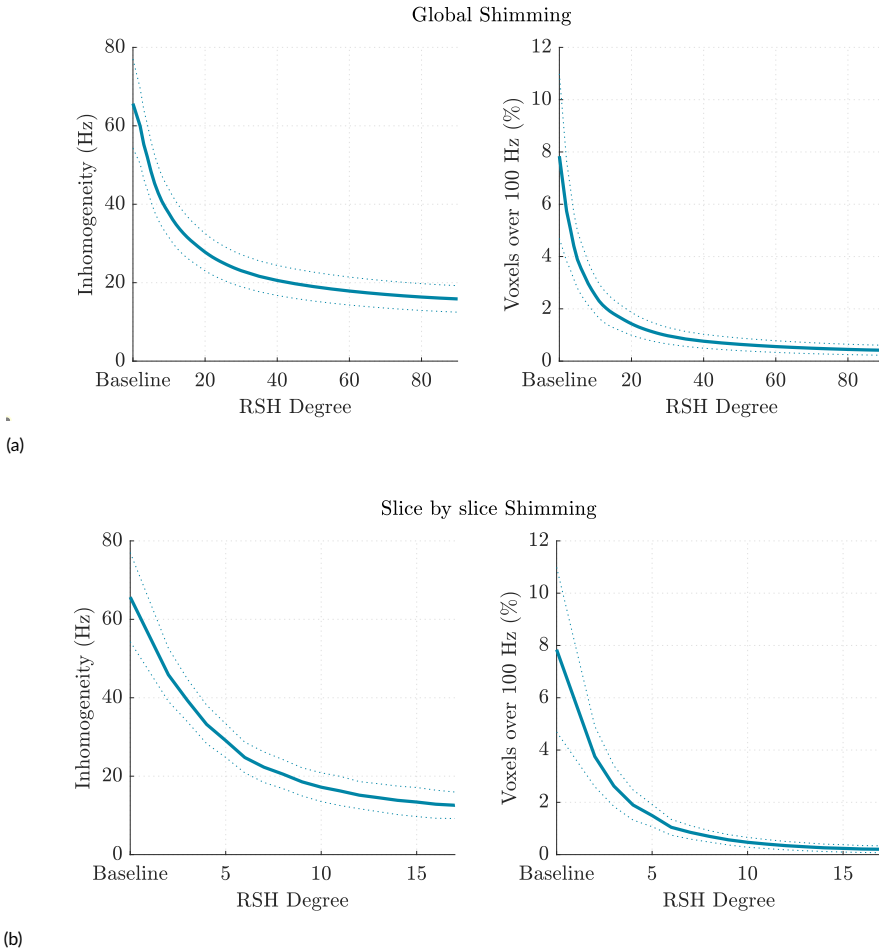


FIGURE 4 Average inhomogeneity and proportion of voxels over 100 Hz across subjects in the database as RSH degree increases (reference field at 7 T). Metrics for each subject are computed considering all voxels in the brain mask after application of (a) global and (b) slice by slice shimming. Dotted lines indicate standard deviation of the metric across subjects in the database.

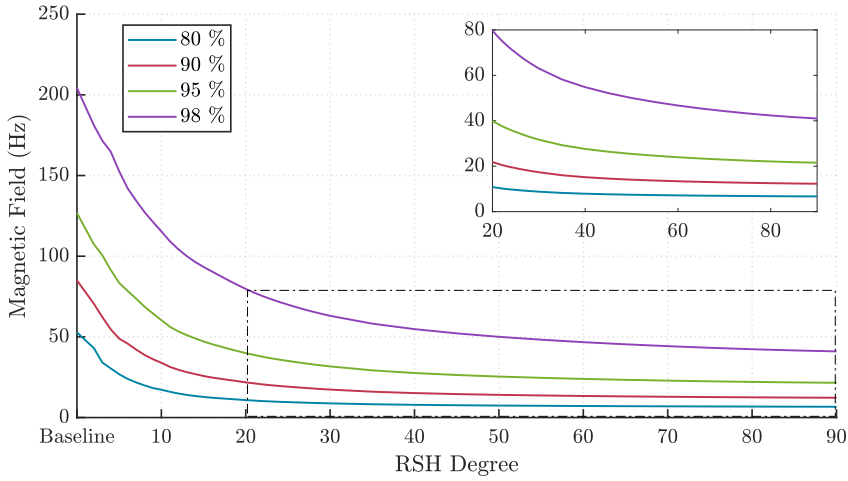


FIGURE 5 Average on the 100-subject database of the absolute frequency range containing 80, 90, 95 and 98 % of voxels in the brain after global shimming as RSH degree increases.

4.3 | Slab Shimming Limits

While slice-by-slice shimming might be unsuited for submillimeter resolution, slab-specific acquisition can be a viable alternative if only a specific region of the brain is of interest. Figs. 7 and 8 show that this shimming modality could also improve homogeneity given a fixed degree of RSH components when compared to what would be achieved in the same ROI under global shimming. Fig.8 shows that at 3rd degree (which is available to limited order in some UHF scanners), localized shimming in specific slabs could provide significant inhomogeneity reduction, with average drops of 7.7 Hz, 9.0 Hz and 8.0 Hz in the PFC and TLs (bilateral and unilateral), respectively. Moreover, considering the TL bilateral slab, when applying global shimming, a 6th degree RSH shim system would be required to provide the same homogeneity as a 3rd degree system if localized shimming was employed. From a hardware perspective, going from 3rd to 6th degree implies adding 33 coils. Therefore, great economy of resources is possible by changing the shimming strategy, provided whole-brain shimming is not an issue. It can also be noticed from the localized shimming simulations that global shimming seems to naturally concentrate efforts in mitigating inhomogeneity in the PFC, as there is a smaller gap in performance and coil number when switching from global to localized shimming. Such smaller relative improvements in the temporal lobes homogeneity has been noticed in several works^{11;24;38}, but as can be seen, could be overcome if localized shimming was employed.

None of the shimming schemes presented so far satisfies the condition for ultimate shimming. In average, the residual inhomogeneity observed in the shimmed ROIs is still superior to 10 Hz.

4.4 | Towards Perfect Shimming in Spherical ROIs

To further study the validity and consequences of the perfect shimming condition, RSH shimming simulations were performed in the four distinct ROIs shown in Fig. 9. We notice how RSH shimming in ROIs 3 and 4, which presumably satisfy the perfect shimming condition, converge faster to lower inhomogeneity values (8.0 Hz and 4.5 Hz, respectively)

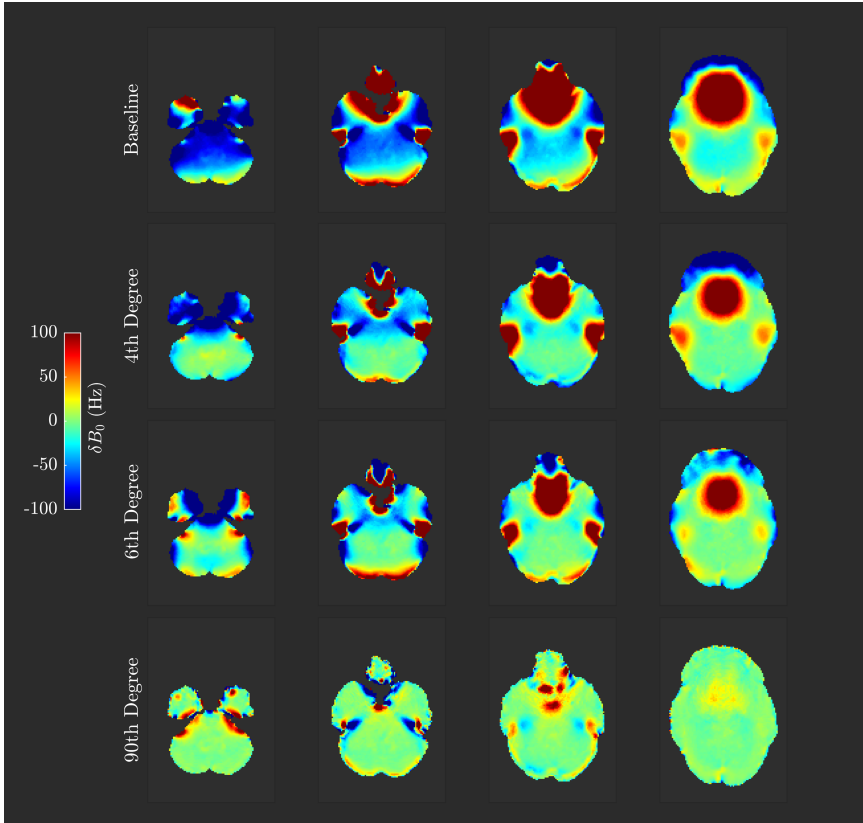


FIGURE 6 Selected axial slices of brain fieldmap after RSH global shimming of different degrees. The slices show zones of high inhomogeneity. 4th and 6th degree fieldmaps are shown as examples of the maximum mitigation levels achieved by shimming systems so far as reported in the literature when performing global shimming. The best inhomogeneity obtained (90th degree shimming) in our unconstrained simulations is also shown.

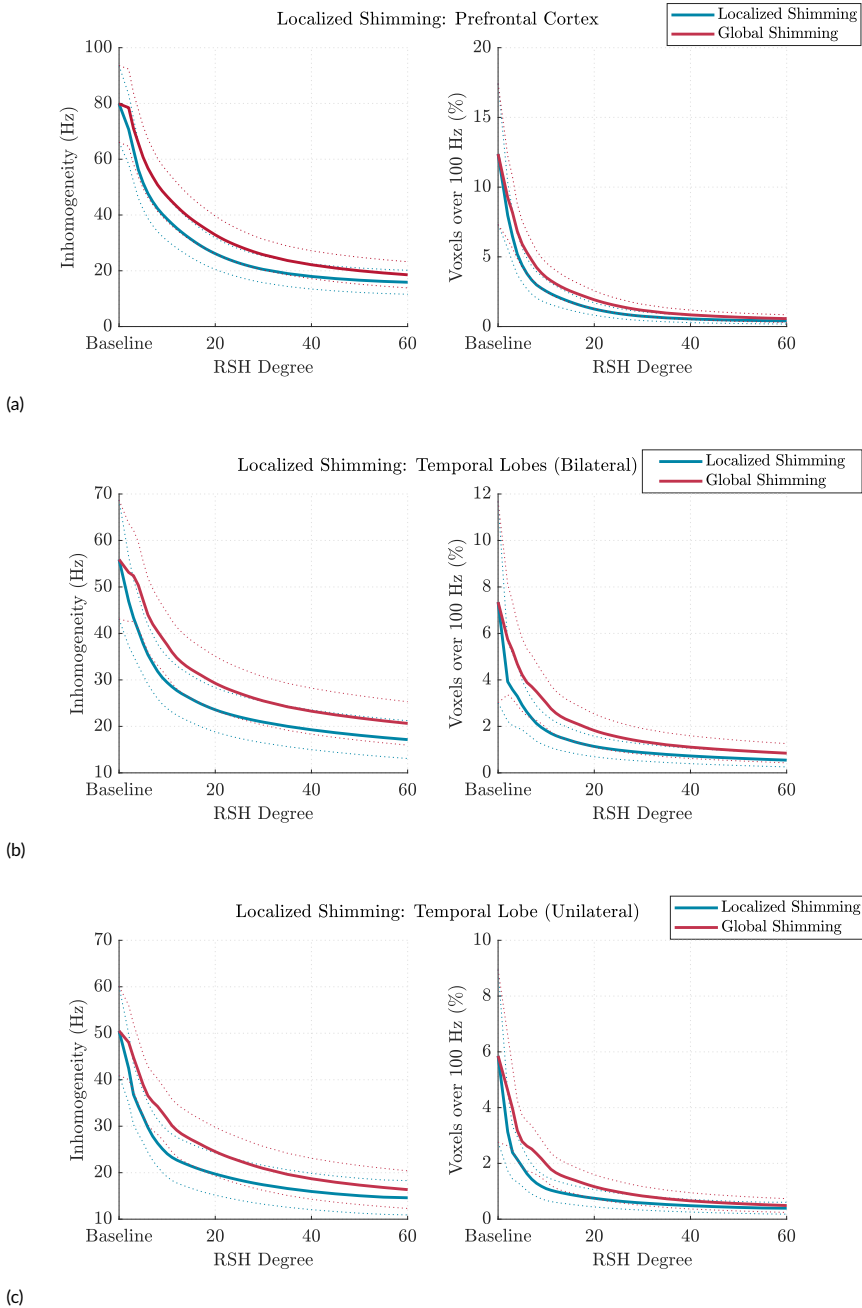
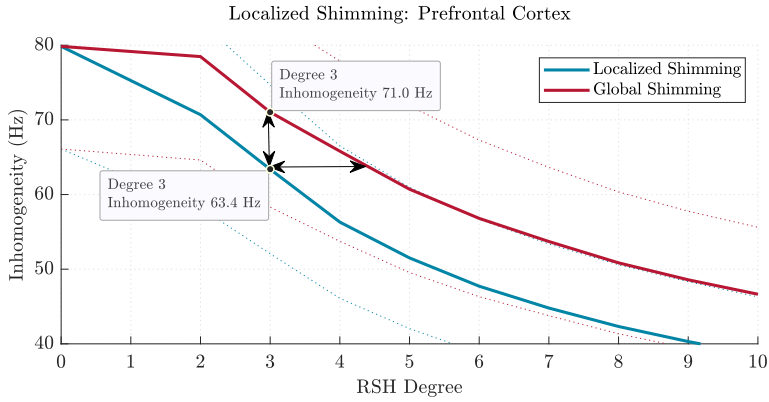
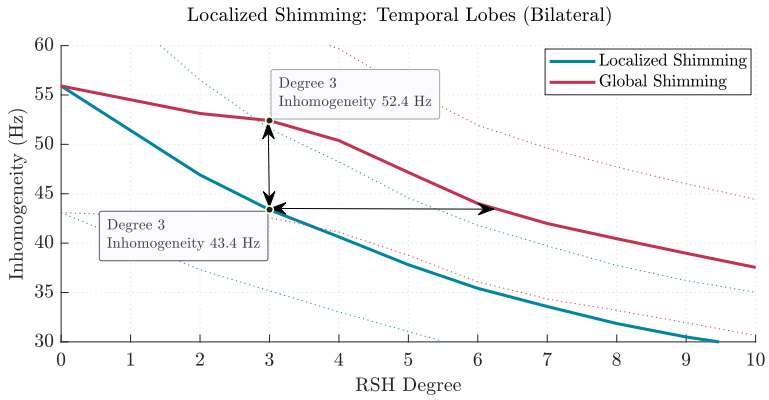


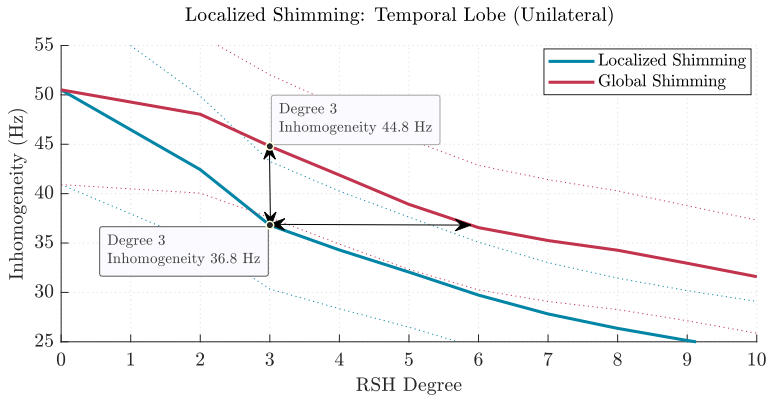
FIGURE 7 Average inhomogeneity and proportion of voxels over 100 Hz across subjects in the database after global and localized RSH shimming of increasing degree. Metrics for each subject are computed considering the voxels inside target slabs enclosing the: (a) prefrontal cortex, (b) both temporal lobes and (c) a single temporal lobe. Dotted lines indicate standard deviation of the metric across subjects in the database.



(a)



(b)



(c)

FIGURE 8 Zoomed depiction of average inhomogeneity across the database in selected slabs for performance comparison between global and localized shimming techniques.

as RSH degree is increased, and present a more localized residual inhomogeneity compared to ROIs 1 and 2 (with final inhomogeneity of 32.7 Hz and 23.0 Hz, respectively). Nevertheless, residual inhomogeneity in ROIs 3 and 4 still remains. These are caused by susceptibility gradients between brain tissues and cannot be zeroed-out. We are also limited by numerical precision to compute infinitely higher-degree coefficients required to shim the excursion hotspots close to the sphere boundaries in ROIs 3 and 4. Moreover, contrarily to intuition, these results also show that fitting the same number of degrees of freedom to a smaller volume does not necessarily mean improved shimming, since despite being the smallest volume, ROI 1 is also the one presenting the largest field excursion in the depicted sagittal slices. Fig. 9c compares the inhomogeneity inside ROI 4 when applying global vs focused shimming: convergence to very low inhomogeneity is seen at 10th degree with localized shimming, versus 50th degree with global shimming.

In terms of the required RSH degree for optimally shimming some region, presented results point to the need of fewer degrees of freedom when employing localized shimming, and these can be further reduced when the shimmed ROI can be positioned inside a sphere non enclosing sources of magnetic field.

4.5 | Optimal Global and Localized Shimming with Power Constraints

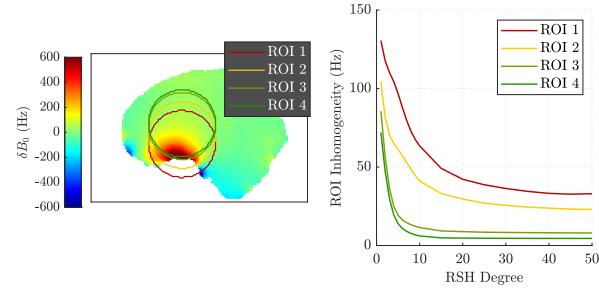
The reduced number of degrees of freedom is a first practical aspect pointing to the advantage of localized shimming. Moreover, by analyzing the inhomogeneity reduction brought by optimal, power-constrained coil designs, the reduced need for RSH degrees in localized shimming translates into improved homogeneity in the target under fixed power dissipation, as observed in Fig. 10.

Inhomogeneity after global shimming with subject-optimal coils at the initial power constraint of 3 W is equivalent to 6th degree RSH shimming. Improvement as power consumption is allowed to increase, however, is mild, reaching an equivalent of a 9th degree RSH shim system at 100 W. As inhomogeneous field distribution becomes more and more localized after mitigation of slower spatially varying patterns, further improvement becomes harder. To address such localized patterns when performing global shimming, small loops with high electric current are needed, thus electric power drastically increases. Such behavior is in accordance with¹⁹, who demonstrates that pure higher degree spherical harmonic patterns are generated by faster spatially varying, thus shorter, winding patterns, at the cost of requiring higher currents.

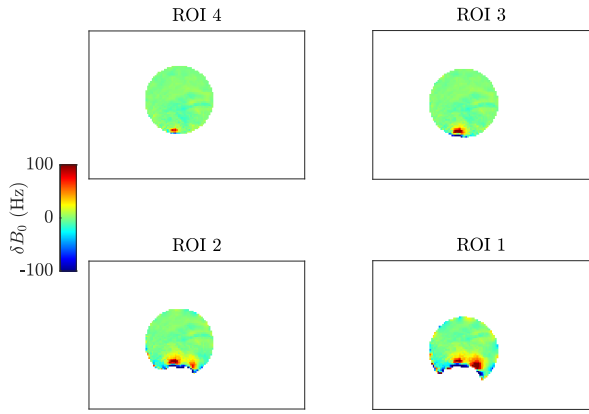
Subject-optimal coil design for localized shimming, however, shows that a significant 17% drop in inhomogeneity can be achieved for the temporal lobes under the same power dissipation constraints with a dedicated system. From the results discussed so far, this is not surprising; for a fixed RSH degree, localized shimming improves the homogeneity in the target compared to global shimming; and since power dissipation is linked to RSH content, employing the same power dissipation in a localized target rather than in global shimming is the equivalent of employing the same amount of RSH degrees in localized versus global shimming. From these results, one could also expect high performance shimming in spherical ROIs satisfying the perfect shimming conditions to be achievable with low power consumption, as the RSH content required to achieve the lowest inhomogeneity in ROI 4, for instance, is of 10th degree, with still very low inhomogeneity at the 6th degree.

We emphasize that the coil design simulation and evaluation had the goal of illustrating how RSH degree content relates to power dissipation. The designed systems are not practical as they imply an optimal coil for each subject. When designing a shim system capable of addressing inter-subject variability, for a fixed power dissipation, performances tend to drop¹³. Nevertheless, these simulations provided evaluation of how power capabilities can be better redirected to improve homogeneity of specific regions of interest.

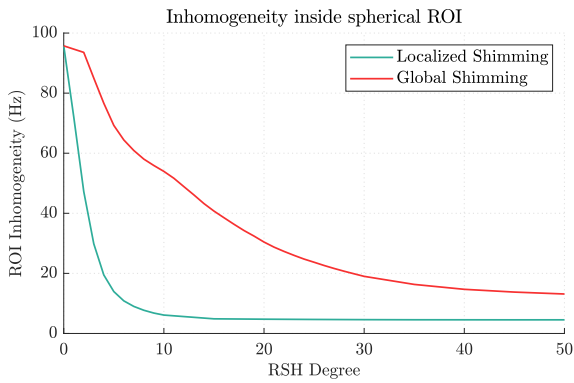
We also note that, despite the low inhomogeneity theoretically achievable in global shimming, in practice such levels of inhomogeneity are probably not achievable since dedicated hardware might not be able to support current



(a)

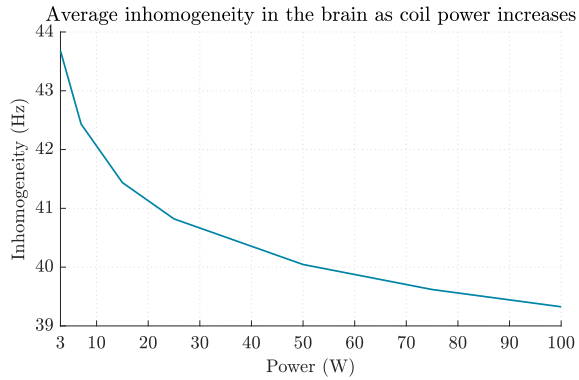


(b)

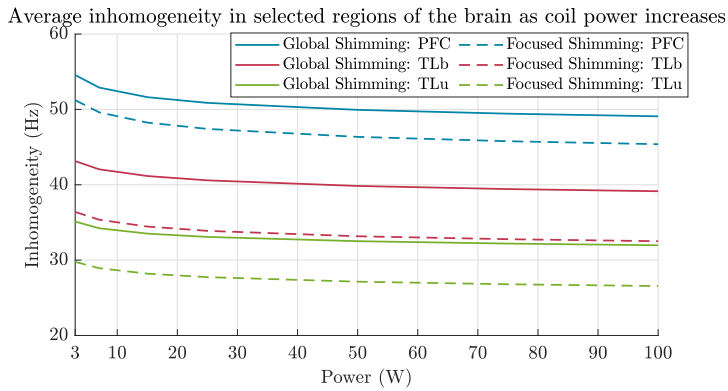


(c)

FIGURE 9 Inhomogeneity assessment after shimming in four spherical ROIs, with ROIs 3 and 4 non-enclosing magnetic field sources, and ROIs 1 and 2 virtually enclosing such sources. Inhomogeneity as RSH degree increases (a) and fieldmap in a sagittal slice after 50th degree shimming (b) are shown. Inhomogeneity evolution inside ROI 4 is also compared under localized and global shimming (c).



(a)



(b)

FIGURE 10 Average inhomogeneity across fieldmaps after subject-optimal coil shimming when designed for (a) global shimming and (b) region-optimized shimming. In (b), dotted lines represent the inhomogeneity obtained with region-specific coils and the solid line represents the inhomogeneity within a specific region after whole-brain shimming optimized coils.

and power levels required to generate the correcting magnetic fields. At 100 W, average inhomogeneity of 39.3 Hz obtained under global shimming is only equivalent to what would be obtained with 9th degree RSH shimming, thus still very far from the estimated lower bound of 12.3 Hz.

Finally, the shimming needs will mainly depend on the robustness of the acquisition sequence to B_0 inhomogeneity. Acquisition schemes such as GRE, MP-RAGE, FSE provide high quality results at 7 T despite conditions that would be harsh for EPI; therefore for those sequences one would not need the best achievable inhomogeneity. For EPI, however, even at 90th degree RSH shimming, leftover inhomogeneity hotspots would still translate into artifacts if no acceleration was used. Again for high-resolution and reduced FOV, localized shimming will facilitate greater shimming performance.

5 | CONCLUSION

The mathematical fundamentals pointing to the impossibility of perfect shimming of the human brain were shown, and unconstrained RSH shimming simulations of very high degree were performed, showing reminiscent regions of high magnetic field excursion at 7 T even at the highest degree simulated, demonstrating the impossibility of perfect shimming of the human brain (12.3 Hz remaining inhomogeneity in average across a 100-subject database). Moreover, an optimized close-to-ideal cylindrical shim coil showed inhomogeneity only comparable to a 9th degree RSH shim system, despite high power dissipation of 100 W. This result helps highlight the difficulty of obtaining high performance shim systems with low power consumption, and sheds light on why, despite efforts developed by many research teams, no system performing better than 6th degree has been prototyped so far.

Localized shimming was shown to provide better homogeneity in a target region than global shimming for a fixed RSH degree. This property was reflected in greater performance of localized shimming under a fixed power dissipation condition.

By judiciously selecting a region to shim such that it satisfies the condition of being enclosed by a sphere not containing sources of magnetic field, very low inhomogeneity can be achieved within relatively low RSH degree, as we observed a faster convergence to the lowest achievable inhomogeneity; in this particular case, the latter is left with lower field excursion caused by less intense susceptibility gradients between tissues composing the brain. We would therefore expect rather low power requirements for shimming systems to achieve almost optimal inhomogeneity in such targets.

Acknowledgements

We would like to thank Nicolas Boulant and Guy Aubert for helpful discussions on this subject. We also thank the CFR Grant funded by the Commissariat à l'Énergie Atomique et aux Énergies Alternatives (CEA).

references

- [1] Rares Salomir, Baudouin Denis de Senneville, and Chrit TW Moonen. A fast calculation method for magnetic field inhomogeneity due to an arbitrary distribution of bulk susceptibility. *Concepts in Magnetic Resonance Part B: Magnetic Resonance Engineering*, 19B(1):26–34, 2003.
- [2] K. M. Lüdeke, P. Röschmann, and R. Tischler. Susceptibility artefacts in NMR imaging. *Magnetic Resonance Imaging*, 3(4): 329–343, January 1985. doi: 10.1016/0730-725X(85)90397-2.

- [3] Peter Jezzard and Robert S. Balaban. Correction for geometric distortion in echo planar images from B0 field variations. *Magnetic Resonance in Medicine*, 34(1):65–73, 1995. doi: 10.1002/mrm.1910340111.
- [4] Yansong Zhao, Adam W. Anderson, and John C. Gore. Computer simulation studies of the effects of dynamic shimming on susceptibility artifacts in EPI at high field. *Journal of Magnetic Resonance*, 173(1):10–22, March 2005. doi: 10.1016/j.jmr.2004.11.009.
- [5] Kevin M. Koch, Douglas L. Rothman, and Robin A. de Graaf. Optimization of static magnetic field homogeneity in the human and animal brain in vivo. *Progress in Nuclear Magnetic Resonance Spectroscopy*, 54(2):69–96, February 2009. doi: 10.1016/j.pnmrs.2008.04.001.
- [6] Travis B Smith and Krishna S Nayak. MRI artifacts and correction strategies. *Imaging in Medicine*, 2(4):445–457, August 2010. doi: 10.2217/iim.10.33.
- [7] Michael Mullen and Michael Garwood. Contemporary approaches to high-field magnetic resonance imaging with large field inhomogeneity. *Progress in Nuclear Magnetic Resonance Spectroscopy*, 120-121:95–108, October 2020. ISSN 00796565. doi: 10.1016/j.pnmrs.2020.07.003. URL <https://linkinghub.elsevier.com/retrieve/pii/S0079656520300261>.
- [8] Christoph Juchem, Terence W. Nixon, Scott McIntyre, Vincent O. Boer, Douglas L. Rothman, and Robin A. de Graaf. Dynamic multi-coil shimming of the human brain at 7T. *Journal of Magnetic Resonance*, 212(2):280 – 288, 2011. ISSN 1090-7807. doi: <https://doi.org/10.1016/j.jmr.2011.07.005>. URL <http://www.sciencedirect.com/science/article/pii/S1090780711002230>.
- [9] Jason Stockmann, Thomas Witzel, J Blau, Jonathan Polimeni, Zhao Wei, B Keil, and Lawrence Wald. Combined shim-rf array for highly efficient shimming of the brain at 7 tesla. *Proc. Int. Soc. Magn. Reson. Med*, 21, January 2013.
- [10] Christoph Juchem, S. Umesh Rudrapatna, Terence W. Nixon, and Robin A. de Graaf. Dynamic multi-coil technique (DYNAMITE) shimming for echo-planar imaging of the human brain at 7 Tesla. *NeuroImage*, 105:462–472, January 2015. ISSN 10538119. doi: 10.1016/j.neuroimage.2014.11.011. URL <https://linkinghub.elsevier.com/retrieve/pii/S1053811914009136>.
- [11] Ali Aghaeifar, Jiazheng Zhou, Rahel Heule, Behzad Tabibian, Bernhard Schölkopf, Feng Jia, Maxim Zaitsev, and Klaus Scheffler. A 32-channel multi-coil setup optimized for human brain shimming at 9.4T. *Magnetic Resonance in Medicine*, 83(2):749–764, February 2020. ISSN 0740-3194, 1522-2594. doi: 10.1002/mrm.27929. URL <https://onlinelibrary.wiley.com/doi/abs/10.1002/mrm.27929>.
- [12] Feng Jia, Hatem Elshatlawy, Ali Aghaeifar, Ying-Hua Chu, Yi-Cheng Hsu, Sebastian Littin, Stefan Kroboth, Huijun Yu, Philipp Amrein, Xiang Gao, Wenchao Yang, Pierre LeVan, Klaus Scheffler, and Maxim Zaitsev. Design of a shim coil array matched to the human brain anatomy. *Magnetic Resonance in Medicine*, 83(4):1442–1457, April 2020. ISSN 0740-3194, 1522-2594. doi: 10.1002/mrm.28016. URL <https://onlinelibrary.wiley.com/doi/abs/10.1002/mrm.28016>.
- [13] Bruno Pinho Meneses and Alexis Amadon. A fieldmap-driven few-channel shim coil design for MRI of the human brain. *Physics in Medicine & Biology*, 66(1), 2020. ISSN 0031-9155. URL <http://iopscience.iop.org/article/10.1088/1361-6560/abc810>.
- [14] L. Van Damme, F. Mauconduit, T. Chambrion, N. Boulant, and V. Gras. Universal nonselective excitation and refocusing pulses with improved robustness to off-resonance for Magnetic Resonance Imaging at 7 Tesla with parallel transmission. *Magnetic Resonance in Medicine*, 85(2):678–693, 2021. ISSN 1522-2594. doi: <https://doi.org/10.1002/mrm.28441>. URL <https://onlinelibrary.wiley.com/doi/abs/10.1002/mrm.28441>.
- [15] Christoph Juchem, Cristina Cudalbu, Robin A. de Graaf, Rolf Gruetter, Anke Henning, Hoby P. Hetherington, and Vincent O. Boer. B0 shimming for in vivo magnetic resonance spectroscopy: Experts' consensus recommendations. *NMR in Biomedicine*, n/a(n/a):e4350, 2020. ISSN 1099-1492. doi: <https://doi.org/10.1002/nbm.4350>. URL <https://onlinelibrary.wiley.com/doi/abs/10.1002/nbm.4350>.

- [16] Alireza Sadeghi-Tarakameh, Lance DelaBarre, Russell L. Lagore, Angel Torrado-Carvajal, Xiaoping Wu, Andrea Grant, Gregor Adriany, Gregory J. Metzger, Pierre-Francois Van de Moortele, Kamil Ugurbil, Ergin Atalar, and Yigitcan Eryaman. In vivo human head MRI at 10.5T: A radiofrequency safety study and preliminary imaging results. *Magnetic Resonance in Medicine*, 84(1):484–496, 2020. ISSN 1522-2594. doi: <https://doi.org/10.1002/mrm.28093>. URL <https://onlinelibrary.wiley.com/doi/abs/10.1002/mrm.28093>.
- [17] Lionel Quettier, Guy Aubert, Jean Belorgey, Christophe Berriaud, Philippe Bredy, Guillaume Dilasser, Olivier Dubois, Graham Gilgrass, Quentin Guihard, Vincent Jannot, Francois-Paul Juster, Herve Lannou, Frederic Molinie, Francois Nunio, Arnaud Roger, Thierry Schild, Loris Scola, Armand Sinanna, Vadim Stepanov, and Pierre Vedrine. Commissioning Completion of the Iseult Whole Body 11.7 T MRI System. *IEEE Transactions on Applied Superconductivity*, 30(4):1–5, June 2020. ISSN 1051-8223, 1558-2515, 2378-7074. doi: 10.1109/TASC.2020.2983702. URL <https://ieeexplore.ieee.org/document/9052451/>.
- [18] Peter A. Bandettini. Twenty years of functional MRI: The science and the stories. *NeuroImage*, 62(2):575–588, August 2012. ISSN 1053-8119. doi: 10.1016/j.neuroimage.2012.04.026. URL <http://www.sciencedirect.com/science/article/pii/S1053811912004223>.
- [19] Françoise Roméo and D. I. Hoult. Magnet field profiling: Analysis and correcting coil design. *Magnetic Resonance in Medicine*, 1(1):44–65, 1984. doi: 10.1002/mrm.1910010107. URL <https://onlinelibrary.wiley.com/doi/abs/10.1002/mrm.1910010107>.
- [20] Robin A. De Graaf. *In vivo NMR spectroscopy: principles and techniques*. John Wiley & Sons, Chichester, West Sussex, England ; Hoboken, NJ, 2nd ed edition, 2007. ISBN 978-0-470-02670-0. OCLC: ocn124036293.
- [21] Andrew Webb, editor. *Magnetic resonance technology: hardware and system component design*. Number 7 in New developments in NMR. Royal Society of Chemistry, Cambridge, UK, 2016. ISBN 978-1-78262-387-8 978-1-78262-359-5 978-1-78262-817-0. OCLC: 933438677.
- [22] Jullie W. Pan, Kai-Ming Lo, and Hoby P. Hetherington. Role of very high order and degree B0 shimming for spectroscopic imaging of the human brain at 7 tesla. *Magnetic resonance in medicine*, 68(4):1007–1017, October 2012. ISSN 1522-2594 0740-3194 0740-3194. doi: 10.1002/mrm.24122.
- [23] Hui Han, Allen W. Song, and Trong-Kha Truong. Integrated parallel reception, excitation, and shimming (iPRES): Integrated Parallel Reception, Excitation, and Shimming. *Magnetic Resonance in Medicine*, 70(1):241–247, July 2013. ISSN 07403194. doi: 10.1002/mrm.24766. URL <http://doi.wiley.com/10.1002/mrm.24766>.
- [24] Ali Aghaeifar, Christian Mirkes, Jonas Bause, Theodor Steffen, Nikolai Avdievitch, Anke Henning, and Klaus Scheffler. Dynamic B0 shimming of the human brain at 9.4 T with a 16-channel multi-coil shim setup. *Magnetic Resonance in Medicine*, 80(4):1714–1725, October 2018. ISSN 0740-3194. doi: 10.1002/mrm.27110. URL <https://doi.org/10.1002/mrm.27110>.
- [25] Bruno Pinho Meneses, Michel Luong, and Alexis Amadon. Optimized multi-coil array design for human brain shimming at Ultra-High Field. In *Proceedings of the 27th Annual Meeting of ISMRM*, page 1477, Montreal, Canada, May 2019.
- [26] Bruno Pinho Meneses and Alexis Amadon. Static-magnetic-field shimming coil system for magnetic resonance imaging, October 2020.
- [27] Bruno Pinho Meneses, Jason Stockmann, and Alexis Amadon. First prototype of a Stream-Function-based Multi-Coil Array dedicated to human brain shimming at Ultra-High-Field. In *Proceedings of the 28th Annual Meeting of ISMRM*, volume 28, page 0766, Virtual, 2020.
- [28] D. F. Hillenbrand, K. M. Lo, W. F. B. Punchard, T. G. Reese, and P. M. Starewicz. High-order MR shimming: a simulation study of the effectiveness of competing methods, using an established susceptibility model of the human head. *Applied Magnetic Resonance*, 29(1):39–64, March 2005. ISSN 0937-9347, 1613-7507. doi: 10.1007/BF03166955. URL <http://link.springer.com/10.1007/BF03166955>.

- [29] J.D. Jackson. *CLASSICAL ELECTRODYNAMICS, 3RD ED.* Wiley India Pvt. Limited, 2007. ISBN 978-81-265-1094-8. URL <https://books.google.fr/books?id=2hZ0CgAAQBAJ>.
- [30] Nikos Makris, Leonardo Angelone, Seann Tulloch, Scott Sorg, Jonathan Kaiser, David Kennedy, and Giorgio Bonmassar. MRI-based anatomical model of the human head for specific absorption rate mapping. *Medical & Biological Engineering & Computing*, 46(12):1239–1251, December 2008. ISSN 0140-0118, 1741-0444. doi: 10.1007/s11517-008-0414-z. URL <http://link.springer.com/10.1007/s11517-008-0414-z>.
- [31] Stephen M. Smith. Fast robust automated brain extraction. *Human Brain Mapping*, 17(3):143–155, November 2002. doi: 10.1002/hbm.10062.
- [32] Shizhe Li, Gerald D. Williams, Timothy A. Frisk, Blake W. Arnold, and Michael B. Smith. A computer simulation of the static magnetic field distribution in the human head. *Magnetic Resonance in Medicine*, 34(2):268–275, 1995. ISSN 1522-2594. doi: <https://doi.org/10.1002/mrm.1910340219>. URL <https://onlinelibrary.wiley.com/doi/abs/10.1002/mrm.1910340219>.
- [33] Martin Kochan, Pankaj Daga, Ninon Burgos, Mark White, M. Jorge Cardoso, Laura Mancini, Gavin P. Winston, Andrew W. McEvoy, John Thornton, Tarek Yousry, John S. Duncan, Danail Stoyanov, and Sébastien Ourselin. Simulated field maps for susceptibility artefact correction in interventional MRI. *International Journal of Computer Assisted Radiology and Surgery*, 10(9):1405–1416, September 2015. ISSN 1861-6429. doi: 10.1007/s11548-015-1253-7. URL <https://doi.org/10.1007/s11548-015-1253-7>.
- [34] Shizhe Li, Bernard J. Dardzinski, Christopher M. Collins, Qing X. Yang, and Michael B. Smith. Three-dimensional mapping of the static magnetic field inside the human head. *Magnetic Resonance in Medicine*, 36(5):705–714, 1996. ISSN 1522-2594. doi: <https://doi.org/10.1002/mrm.1910360509>. URL <https://onlinelibrary.wiley.com/doi/abs/10.1002/mrm.1910360509>.
- [35] Christopher M. Collins, Bei Yang, Qing X. Yang, and Michael B. Smith. Numerical calculations of the static magnetic field in three-dimensional multi-tissue models of the human head. *Magnetic Resonance Imaging*, 20(5):413–424, June 2002. ISSN 0730-725X. doi: 10.1016/S0730-725X(02)00507-6. URL <http://www.sciencedirect.com/science/article/pii/S0730725X02005076>.
- [36] Jiazheng Zhou, Jason P. Stockmann, Nicolas Arango, Thomas Witzel, Klaus Scheffler, Lawrence L. Wald, and Fa-Hsuan Lin. An orthogonal shim coil for 3T brain imaging. *Magnetic Resonance in Medicine*, 83(4):1499–1511, April 2020. ISSN 0740-3194, 1522-2594. doi: 10.1002/mrm.28010. URL <https://onlinelibrary.wiley.com/doi/10.1002/mrm.28010>.
- [37] Kevin M. Koch, Scott McIntyre, Terence W. Nixon, Douglas L. Rothman, and Robin A. de Graaf. Dynamic shim updating on the human brain. *Journal of Magnetic Resonance*, 180(2):286–296, June 2006. ISSN 1090-7807. doi: 10.1016/j.jmr.2006.03.007. URL <https://www.sciencedirect.com/science/article/pii/S109078070600067x>.
- [38] Jason P. Stockmann and Lawrence L. Wald. In vivo B 0 field shimming methods for MRI at 7 T. *NeuroImage*, 168:71–87, March 2018. ISSN 10538119. doi: 10.1016/j.neuroimage.2017.06.013. URL <https://linkinghub.elsevier.com/retrieve/pii/S1053811917304822>.